

Eccentricity Detection of a Six Phase Induction Motor with High Frequency Injection

ISSN 1751-8644
 doi: 0000000000
www.ietdl.org

Tong Wang¹, Jin Huang^{1*}, Benhong Lin¹, Min Kang², Jiahao Chen¹, Wubin Kong³

¹ Department of Electrical Engineering, Zhejiang University, Hangzhou, China

² Fusheng Electrical Appliance Co. Ltd., Hangzhou, China

³ School of Electrical and Electronic Engineering, Huazhong University of Science and Technology, Wuhan, China

* E-mail: ee_huangj@emb.zju.edu.cn

Abstract: Eccentricity detection is an important topic in motor fault diagnosis and bearingless motor controls. In this paper, a novel method is proposed for eccentricity detection of a six phase motor based on high frequency injection (HFI). Unlike the other planes of the multiphase motors, the 0_{-} component (the average of the differences between adjacent phases) is seldom adopted for signal injections. The proposed method exploits the 0_{-} component for signal injection which allows the injected signals to be decoupled from the rotating-magnetic-field-producing planes without occupying any of them (so that they can be assigned to other uses). In this paper, the induction motor under HFI is simplified as a model with mutually decoupled winding pairs. The high frequency impedance of each phase under eccentricity is derived on the basis of this model. The proposed method is drawn from these theories and verified with experiments. It is shown in the experiments that the proposed method has excellent linearity; the estimations on orthogonal directions are decoupled; the proposed method has satisfactory tracking bandwidth. The influence of saturation on the proposed method is justified by simulations. The capability of the proposed method to discriminate between different types of eccentricities is proved with experimental data.

Nomenclature

γ	Radial displacement angle relative to α axis
d_{α}, d_{β}	Radial displacements on α and β directions
$\hat{d}_{\alpha}, \hat{d}_{\beta}$	Estimated radial displacements on α and β directions
g_0	Effective length of air gap
$\tilde{d}_{\alpha}, \tilde{d}_{\beta}$	$\hat{d}_{\alpha} - d_{\alpha}$ and $\hat{d}_{\beta} - d_{\beta}$
g_0	Effective length of air gap
ϕ_a, ϕ_b, ϕ_c	Angular directions of winding axes of Phase A, B, C
ϕ_d, ϕ_e, ϕ_f	Angular directions of winding axes of Phase D, E, F
Subscript c	Carrier signal related
Superscript inj	Injected signal
Superscript '	Image winding

1 Introduction

Eccentricity detection is an important topic in motor fault diagnosis. Common motors have inherent eccentricities due to imperfect manufacturing and inaccurate rotor dynamic balancing [1, 2]. When the eccentricities are worsened by ill performances, larger unbalanced magnetic pulls and severer eccentricities arise [3]. Consequently, larger vibrations occur [3] and the risks of mechanical interference between the rotor and the stator increase. Since on-line access to the rotors is hardly possible, eccentricity detections using the electrical quantities (voltages and currents) become necessary [4]. In order to discover the eccentricity faults in early stages, numerous fault diagnosing methods have been proposed. The most commonly used and sophisticated method is the motor current signature analysis (MCSA) [5, 6]. However, the MCSA is not capable of discriminating dynamic and static eccentricities [7], especially when rotor slot harmonics are very small. Moreover, the MCSA can only deal with steady state operations. Although finite element analysis and pattern recognition methods have been introduced to extend the use of MCSA to transient operations [3, 4, 8, 9], these methods are quite time consuming. Hence, signal injection based methods were proposed in [1, 2] to detect the eccentricity under transient operation.

Eccentricity detections are also important in bearingless motor controls. If the radial displacements of the rotor can be estimated, the length of the machine can be shortened because of the elimination of the displacement sensors and the standard plate [10]. The cost of the system will also be reduced. Moreover, when the motor enters high speed range where the shaft start to vibrate, the radial displacements of the standard plate will be different from the radial displacements of the rotor core. Adopting the eccentricity detection method to estimate the radial displacements of the rotor core will solve this problem [10]. In [11], the midpoint voltages of the torque producing windings are adopted as indicators of the radial displacements. However, this method can only be applied to two-phase motors and requires tapping leads on the midpoints with additional voltage sensors to measure the indicators. Moreover, this method requires two identical large resistors to obtain a reference point for the midpoint voltages. However, resistance values of large resistors can hardly be accurate in practice. If the resistors are not identical, there will be offsets introduced in the displacement indicators from the reference point. In [12], high frequency (HF) signals are injected in the torque producing winding of the bearingless motor, and the mutual inductances between the torque producing winding and the suspension winding are detected. Since the mutual inductances are proportional to the radial displacements, the eccentricity condition can be detected. Because this method injects the HF signals in the torque producing winding, the extraction of the radial displacements from the carrier signals must deal with the fundamental waves for suspension force producing. In [13, 14], search coils are embedded in the stator slots to detect the eccentricity of the rotor. This method only faces fundamental disturbances under saturation, but requires extra manufacturing processes during coil assembling.

It can be found from above that the signal injection based eccentricity detection methods are paid more and more attention, especially when the eccentricities need to be detected under transient operations. However, because motor windings are assigned to certain purposes, such as torque producing or suspension force producing, injecting extra signals in them will inevitably influence their normal

operations. On the other hand, the fundamental voltages and currents of the windings must be dealt with when extracting information from the carrier signals. If the problems mentioned above need to be avoided, extra coils should be added (search coils in [13, 14] for example).

It is not the case in the multiphase motors. Multiphase machines have additional degrees of freedom (DOF) which are suitable for either controls or estimations [15, 16]. These additional DOFs can be mapped onto decoupled planes which are able to produce rotating magnetic field (MF) of different pole pairs. These planes are equivalent to multiple windings which are mutually independent. They can be used to realize many applications, such as fault tolerant control [17], fault diagnosis [18], non-sinusoidal powering and flux distribution optimization [19, 20], sensorless drive [21] and bearingless drive [22, 23]. For signal injection based algorithms, the multiphase machines can also provide decoupled signal injection spaces [21], only that injecting signals in these equivalent windings take the place where other applications could have been embedded. Among all the decoupled planes and axes, the zero sequence plane ($0_+ - 0_-$ plane) [15] cannot produce rotating MFs because neutral wires do not always exist. The 0_+ component is the zero sequence component in the general meaning. Without a neutral wire, it is not available for any currents to pass. The 0_- component is the average of the differences between adjacent phases. It only exists in machines of even phase numbers. But the 0_- component allows currents to pass without any additional wires. Moreover, it is capable of producing pulsating MF when provided with alternating currents. This is adequate for signal injection based estimations. Most importantly, it allows decoupled signal injection without occupying rotating-MF-producing planes which can be assigned to other uses.

In this paper, a novel eccentricity detection method is proposed for a six phase motor. The HF signal is injected in the 0_- component. When injecting HF signals in an induction motor (IM), an important feature was neglected by many existing literatures [12–14]. It is the fact that the MF produced by the HF currents cannot penetrate into the rotor iron core because of the counteracting induced currents in the rotor bars [24, 25]. The same phenomenon also appears in an eddy current displacement probe (ECDP), where the HFMF of the ECDP cannot penetrate into the target metal surface. Based on this phenomenon, the ECDP can detect displacements from its own impedance [26, 27]. This displacement detection principle is adopted in the IM in the proposed method. Under HF excitations, the IM is simplified to a model with decoupled winding pairs according to the method of images [28]. These winding pairs are just like the transformer models of the ECDPs. Based on this simplified model, the HF impedance of a single phase under eccentricity is developed. To obtain the radial displacements from the impedances, the proposed method adopts an orthogonal generation system (OGS) based demodulation strategy to extract the current amplitudes (determined by the impedance). It will be proved in the experiments that the proposed method has excellent linearity, the estimations in orthogonal directions are decoupled and the tracking bandwidths are satisfactory.

This paper is organized as follows: In Section II, the decoupled signal injection on the 0_- axis is presented and the HF impedance of a certain phase under eccentricity is derived based on the simplified IM model with decoupled winding pairs. In Section III, the eccentricity detection method is proposed based on the impedance theory as well as a demodulation strategy based on the OGS. In Section IV, simulations are carried out to justify the influence of saturation on the proposed method, experiments are carried out under static and dynamic conditions to verify the accuracy of the proposed method, experiment data from two kinds of mixed eccentricities are analyzed under two frequencies to prove the capability of the proposed method to discriminate between dynamic and static experiments. It is proved that the proposed method has excellent linearity and satisfactory bandwidth. In Section V, the conclusions are drawn.

2 Decoupled HFI in an Eccentric Six Phase IM

2.1 Decoupled Signal Injection

The Clarke's transformation of a six phase motor is as (1) and (2) [15, 29],

$$\begin{bmatrix} \underbrace{i_{\alpha_1} & i_{\beta_1}}_{\alpha_1 - \beta_1 \text{ plane}} & \underbrace{i_{\alpha_2} & i_{\beta_2}}_{\alpha_2 - \beta_2 \text{ plane}} & \underbrace{i_{0_+} & i_{0_-}}_{0_+ - 0_- \text{ plane}} \end{bmatrix}^T = T \begin{bmatrix} i_a \\ i_b \\ i_c \\ i_d \\ i_e \\ i_f \end{bmatrix} \quad (1)$$

$$T = \sqrt{\frac{1}{3}} \begin{bmatrix} 1 & \cos \xi & \cos 2\xi & \cos 3\xi & \cos 4\xi & \cos 5\xi \\ 0 & \sin \xi & \sin 2\xi & \sin 3\xi & \sin 4\xi & \sin 5\xi \\ 1 & \cos 2\xi & \cos 4\xi & \cos 6\xi & \cos 8\xi & \cos 10\xi \\ 0 & \sin 2\xi & \sin 4\xi & \sin 6\xi & \sin 8\xi & \sin 10\xi \\ \frac{1}{\sqrt{2}} & \frac{1}{\sqrt{2}} & \frac{1}{\sqrt{2}} & \frac{1}{\sqrt{2}} & \frac{1}{\sqrt{2}} & \frac{1}{\sqrt{2}} \\ \frac{1}{\sqrt{2}} & -\frac{1}{\sqrt{2}} & \frac{1}{\sqrt{2}} & -\frac{1}{\sqrt{2}} & \frac{1}{\sqrt{2}} & -\frac{1}{\sqrt{2}} \end{bmatrix} \quad (2)$$

where $\xi = \pi/3$. From (1) and (2), it can be found that the six phase currents of the motor can be mapped into three orthogonal planes which are mutually independent. While the $\alpha_1 - \beta_1$ and $\alpha_2 - \beta_2$ planes are frequently exploited for extension of control or estimation degrees of freedom (DOF), the $0_+ - 0_-$ plane is seldom paid attention to. Unlike the 0_+ component, the 0_- component allows currents to pass without a neutral wire, and it is capable of producing pulsating MF when provided an alternating excitation with some extra losses due to connections of the two three phase winding sets. Therefore, it is a perfect place for signal injection because extra signals on the 0_- axis will not affect any existing algorithms in the $\alpha_1 - \beta_1$ and $\alpha_2 - \beta_2$ planes and the features of the eccentric rotor can also be excited by the pulsating MF. The injected signals are as (3), where V_c and ω_c are the amplitude and angular speed of the injected carrier signal.

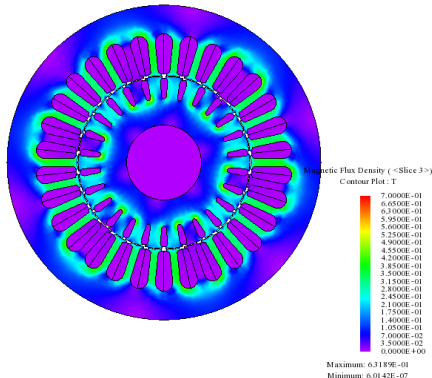
$$\begin{bmatrix} u_a^{inj} & u_b^{inj} & u_c^{inj} & u_d^{inj} & u_e^{inj} & u_f^{inj} \end{bmatrix} = V_c \begin{bmatrix} \sin \omega_c t \\ -\sin \omega_c t \\ \sin \omega_c t \\ -\sin \omega_c t \\ \sin \omega_c t \\ -\sin \omega_c t \end{bmatrix}^T \quad (3)$$

2.2 The HF Signals in an IM

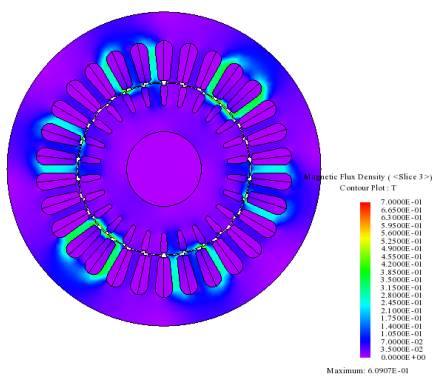
The squirrel cage of an IM acts as a shielding layer when HF currents are applied in the stator windings. The HFMF created by the HF rotor currents cancels the HFMF created by the HF stator currents. Therefore, the HFMF cannot penetrate into the rotor iron core [24, 25]. An illustration of the differences between low frequency and high frequency MF in an IM is presented in Fig.1.

To simplify the analysis of an IM under HF excitations, the IM rotor will be regarded as a non-salient iron core with a layer of conductor at the rotor surface (the approximate equivalent of the rotor cage) as Fig.2(a). Further, according to the method of images [28], the HF rotor currents are equivalent to the images of the stator currents (symmetric to the stator currents with respect to the surface of the conductor layer as Fig.2(b)). These image currents form image windings of the stator windings.

According to the Lenz's law, the stator currents and their image currents counteract each other. Therefore, the coupling effects between winding pairs (consists of the stator winding and its image winding) of different phases become minimal. To elaborate this principle, Fig.3 is presented. In Fig.3, the winding pairs of Phase x and Phase y are presented. When a high frequency current is applied in Winding x, an image winding (Winding x') appears in the rotor. The air-gap magnetic fields produced by Winding x and Winding x' are denoted as $B_x(\theta)$ and $B_{x'}(\theta)$, where θ is the angular



(a)



(b)

Fig. 1: Illustrations of the MF in a six phase motor under current excitation on 0₋ axis. (a) 1 Hz. (b) 200 Hz.

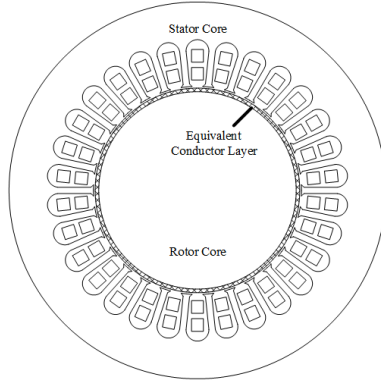
spacial position along the air-gap. Because Winding x and Winding x' counteract each other, when the frequency is high enough, $(B_x(\theta)) \approx -B_{x'}(\theta)$. Hence, the influences of Winding x on Winding y and y' (red lines in Fig.3) are cancelled out by the influences of Winding x' (black lines in Fig.3). Further, it can be derived that the influences of Winding y and y' cancel each other out on Winding x and x' . Hence, under high frequency excitations, the winding pairs of different phases become decoupled, and the model of an IM under HF excitations on 0₋ axis can be simplified as a model with decoupled winding pairs as Fig.4.

Using the IM model with decoupled winding pairs, the analysis of rotor eccentricity can be carried out on every individual phases. In Fig.5, a single winding pair in an eccentric motor is drawn. Such a winding pair is similar to the transformer model of an ECDP [26, 27]. Therefore, the winding pair of Phase x (x can be a, b, c, d, e, f) can be written as a transformer model as (4) [26, 27],

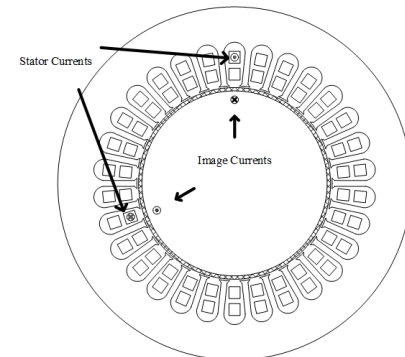
$$\begin{bmatrix} U_{sx} \\ 0 \end{bmatrix} = \begin{bmatrix} R_s + j\omega_c L_{sx} & -j\omega_c M_x \\ -j\omega_c M_x & R_r + j\omega_c L_{rx} \end{bmatrix} \begin{bmatrix} I_{sx} \\ I_{rx} \end{bmatrix} \quad (4)$$

where U_{sx} , I_{sx} and I_{rx} are phasors of the stator terminal voltage, stator current and rotor image current in Phase x; R_s and R_r are the stator resistance and rotor resistance (image winding) of a single phase; L_{sx} , L_{rx} and M_x are the stator inductance, rotor inductance (image winding), and mutual inductance between stator winding and rotor winding (image winding) in Phase x. From (4), the impedance of Phase x can be derived as (5).

$$Z_x = \frac{U_{sx}}{I_{sx}} = \left[R_s + \frac{\omega_c^2 M_x^2 R_r}{R_r^2 + \omega_c^2 L_{rx}^2} \right] + j \left[\omega_c L_{sx} - \frac{\omega_c^3 M_x^2 L_{rx}}{R_r^2 + \omega_c^2 L_{rx}^2} \right] \quad (5)$$



(a)



(b)

Fig. 2: Illustration of the simplifications of an IM under HF excitations. (a) The simplified cage rotor model with a layer of conductor at the surface. (b) The image currents in the rotor of the stator currents under HF.

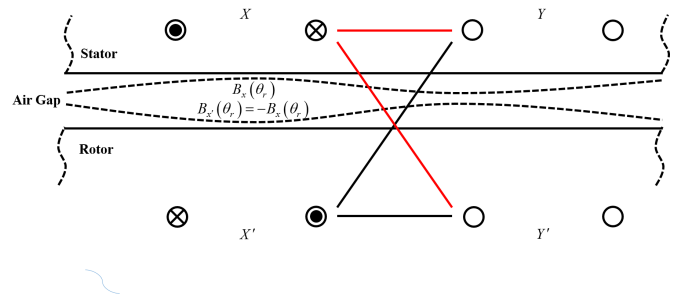


Fig. 3: Illustration of the decoupled winding pairs of each phases.

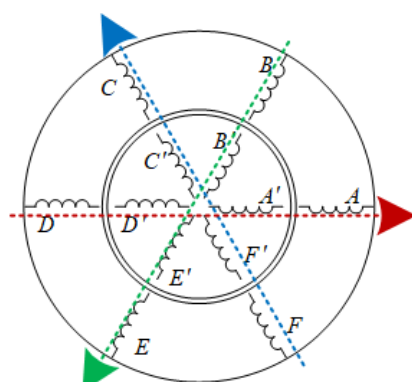


Fig. 4: IM model with decoupled winding pairs under high frequency excitations.

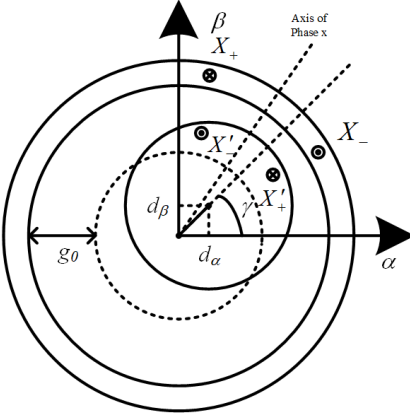


Fig. 5: Illustration of a single winding pair under rotor eccentricity.

Considering that the injected signal frequency is quite high, (5) can be approximated with (6).

$$Z_x \approx j \left[\omega_c L_{sx} - \frac{\omega_c^3 M_x^2 L_{rx}}{R_r^2 + \omega_c^2 L_{rx}^2} \right] \quad (6)$$

2.3 Impedance Analysis under Eccentricity

The impedance (Z_x) under eccentricity is analyzed with the winding function theory [22, 23, 30, 31]. L_{sx} , L_{rx} , and M_x will be calculated with (7).

$$L_{xy} = 2\pi\mu_0 lr \langle P(\theta_r) N_x N_y \rangle - 2\pi\mu_0 lr \frac{\langle P(\theta_r) N_x \rangle \langle P(\theta_r) N_y \rangle}{\langle P(\theta_r) \rangle} \quad (7)$$

The operator $\langle f \rangle$ is defined as the mean of function f over $[0, 2\pi]$ range as follows:

$$\langle f \rangle = \frac{1}{2\pi} \int_0^{2\pi} f(\tau) d\tau$$

L_{xy} is the mutual inductance between Winding x and Winding y ; N_x and N_y are the winding functions of Winding x and Winding y ; $P(\theta_r)$ is the distribution of inverse of airgap with respect to the angular position θ_r ; μ_0 is the vacuum permeability; l and r are the radius and axial length of the rotor core. Under eccentricity, $P(\theta_r)$ can be approximated as (8) [11–13, 22, 23, 32], where $\rho = \sqrt{d_\alpha^2 + d_\beta^2}/g_0$ is the eccentricity ratio.

$$P(\theta_r) = \frac{1}{g_0} + \frac{1}{g_0^2} (d_\alpha \cos(\theta_r) + d_\beta \sin(\theta_r)) = \frac{1 + \rho \cos(\theta_r - \gamma)}{g_0} \quad (8)$$

The winding functions of the image winding and the stator winding should be identical as (9), where N_1 , N_2 , N_3 are the 1st, 2nd and 3rd order harmonic coefficients of the winding function; ϕ_x is the axis angle of Phase x relative to the α axis.

$$N_x = N_{x'} = N_1 \cos(\theta_r - \phi_x) + N_2 \cos(2\theta_r - 2\phi_x) + N_3 \cos(3\theta_r - 3\phi_x) \quad (9)$$

Therefore, L_{sx} , L_{rx} and M_x can be expressed as (10) [32].

$$\begin{aligned} L_{sx} &= L_{rx} = M_x \\ &= 2\pi\mu_0 lr \left\langle P(\theta_r) N_x^2 \right\rangle - 2\pi\mu_0 lr \frac{\langle P(\theta_r) N_x \rangle^2}{\langle P(\theta_r) \rangle} \\ &= 2\pi\mu_0 lr \left\langle P(\theta_r) N_{x'}^2 \right\rangle - 2\pi\mu_0 lr \frac{\langle P(\theta_r) N_{x'} \rangle^2}{\langle P(\theta_r) \rangle} \\ &= 2\pi\mu_0 lr \langle P(\theta_r) N_x N_{x'} \rangle - 2\pi\mu_0 lr \frac{\langle P(\theta_r) N_x \rangle \langle P(\theta_r) N_{x'} \rangle}{\langle P(\theta_r) \rangle} \\ &= W_1 + W_2 \end{aligned} \quad (10)$$

$$W_1 = \frac{\mu_0 lr}{g_0} (N_1^2 + N_2^2 + N_3^2)$$

$$W_2 = \frac{\mu_0 lr}{g_0} \{ \rho (N_1 N_2 + N_2 N_3) \cos(\gamma - \phi_x) + o(\rho) \}$$

$o(\rho)$ is the higher order infinitesimal with respect to ρ . From (6) and (10), the modulus of the admittance of Phase x is as (11).

$$|Y_x| = \left| \frac{1}{Z_x} \right| \approx \frac{1}{\omega_c (W_1 + W_2) - \frac{\omega_c^3 (W_1 + W_2)^3}{R_r^2 + \omega_c^2 (W_1 + W_2)^2}} \quad (11)$$

Linearize (11) with respect to W_2 at $W_2 = 0$. It yields (12).

$$|Y_x| \approx \frac{R_r^2 + \omega_c^2 W_1^2}{\omega_c W_1 R_r^2} - \frac{R_r^2 - \omega_c^2 W_1^2}{\omega_c W_1^2 R_r^2} W_2 \quad (12)$$

Further, neglecting the higher order infinitesimal in W_2 , (13) can be found.

$$|Y_x| \approx \frac{R_r^2 + \omega_c^2 W_1^2}{\omega_c W_1 R_r^2} - W_3 \rho \cos(\gamma - \phi_x) \quad (13)$$

where

$$W_3 = \frac{\mu_0 lr (R_r^2 - \omega_c^2 W_1^2) (N_1 N_2 + N_2 N_3)}{\omega_c W_1^2 R_r^2 g_0}$$

is the incremental impedance added to the normal impedance of Phase x (concentric rotor), when the rotor surface touches the stator inner surface at the center of Phase x ($\gamma = \phi_x$, $\rho = 1$).

3 Eccentricity Detection with Signal Injection

From the last section, it is revealed that the admittance of a winding under HF excitation is related to the eccentricity. In this section, the method to detect the eccentricity (rotor radial displacement) is proposed.

3.1 Basic Principles

Consider a Phase z, which is in the opposite direction to Phase x (Phase D to Phase A for instance). Its admittance will be (14).

$$|Y_z| \approx \frac{R_r^2 + \omega_c^2 W_1^2}{\omega_c W_1 R_r^2} - W_3 \rho \cos(\gamma - \phi_x + \pi) \quad (14)$$

Hence,

$$|Y_x| - |Y_z| = -2W_3 \rho \cos(\gamma - \phi_x) \quad (15)$$

When the signals as (3) is injected, the displacement in ϕ_x direction can be calculated as (16).

$$\sqrt{d_\alpha^2 + d_\beta^2} \cos(\gamma - \phi_x) = \frac{-g_0}{2W_3 V_c} (|I_x| - |I_z|) \quad (16)$$

From (16), the radial displacements in the directions of ϕ_a , ϕ_c and ϕ_e can be obtained as follows:

$$\sqrt{d_\alpha^2 + d_\beta^2} \cos(\gamma) = \frac{-g_0}{2W_3 V_c} (|I_A| - |I_D|) \quad (17)$$

$$\sqrt{d_\alpha^2 + d_\beta^2} \cos\left(\gamma - \frac{2\pi}{3}\right) = \frac{-g_0}{2W_3 V_c} (|I_C| - |I_F|) \quad (18)$$

$$\sqrt{d_\alpha^2 + d_\beta^2} \cos\left(\gamma + \frac{2\pi}{3}\right) = \frac{-g_0}{2W_3 V_c} (|I_E| - |I_B|) \quad (19)$$

(17), (18) and (19) are the radial displacements in the directions of red, blue and green dashed arrows in Fig. 4. Therefore, analogous to

the three phase Clarke's transformation, the radial displacement in the $\alpha - \beta$ frame can be calculated as (20) and (21).

$$\begin{aligned} d_\alpha &= \frac{-g_0}{2W_3V_c} (|I_A| - |I_D|) \\ &+ \frac{-g_0}{2W_3V_c} (|I_C| - |I_F|) \cos\left(\frac{2\pi}{3}\right) \\ &+ \frac{-g_0}{2W_3V_c} (|I_E| - |I_B|) \cos\left(-\frac{2\pi}{3}\right) \quad (20) \\ &= \frac{-g_0}{2W_3V_c} [|I_A| - |I_D|] \\ &+ \frac{1}{2} (|I_B| - |I_C| - |I_E| + |I_F|) \end{aligned}$$

$$\begin{aligned} d_\beta &= \frac{-g_0}{2W_3V_c} (|I_C| - |I_F|) \sin\left(\frac{2\pi}{3}\right) \\ &+ \frac{-g_0}{2W_3V_c} (|I_E| - |I_B|) \sin\left(-\frac{2\pi}{3}\right) \quad (21) \\ &= \frac{-\sqrt{3}g_0}{4W_3V_c} (|I_B| + |I_C| - |I_E| - |I_F|) \end{aligned}$$

3.2 Demodulation Strategy

It can be found from (20) and (21) that radial displacements (d_α and d_β) are modulated in the amplitude of the HF currents. To demodulate the HF current and obtain their amplitudes, an OGS as shown in Fig.6(a) is adopted [33]. The OGS consists of two filters as (22) and (23) where i_x^d and i_x^q are the direct and quadrature components produced by the OGS.

$$H_d(s) = \frac{i_x^d}{i_x} = \frac{G\omega_c s}{s^2 + G\omega_c s + \omega_c^2} \quad (22)$$

$$H_q(s) = \frac{i_x^q}{i_x} = \frac{G\omega_c^2}{s^2 + G\omega_c s + \omega_c^2} \quad (23)$$

The bode diagrams of $H_d(s)$ and $H_q(s)$ are depicted in Fig.6(b). From Fig.6(b), it can be found that $H_q(s)$ has a 90 degree phase displacement at ω_c . Consequently, its output can serve as the orthogonal signal. Moreover, it can also be found that the attenuation of $H_d(s)$ and $H_q(s)$ are unity at ω_c . Namely, i_x^d and i_x^q preserve the amplitude information of i_x . It should be noted that $H_q(s)$ does not attenuate the low frequency disturbances according to the Bode diagram. Such low frequency disturbances include the fundamental frequency components. Therefore, it is necessary for the two filters to connect in series as in Fig.6(a), so that the low frequency disturbances will be suppressed by $H_d(s)$ first. From i_x^d and i_x^q , (24) can be used to obtain the current amplitude.

$$|i_x| = \sqrt{(i_x^d)^2 + (i_x^q)^2} \quad (24)$$

With the demodulation strategy above, $|I_A|, |I_B|, |I_C|, |I_D|, |I_E|, |I_F|$ can be obtained. Using (20) and (21), the radial displacements can be found. The system diagram of the eccentricity detection process is presented in Fig.6(c).

4 Simulation and Experiment Results

4.1 Simulation Results

In this subsection, finite element method (FEM) is used to verify the influence of saturation on the proposed eccentricity detection method. The proposed method is simulated under linear and saturated conditions.

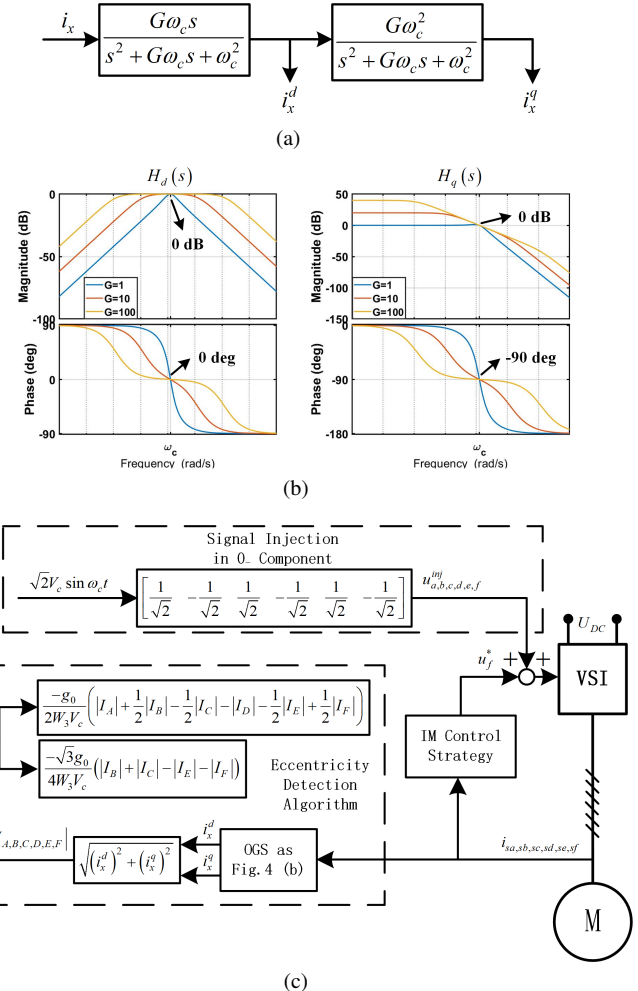


Fig. 6: Illustration of the eccentricity detection process. (a) Bode diagrams of $H_d(s)$ and $H_q(s)$. (b) Block diagram of the OGS. (c) System diagram of the eccentricity detection.

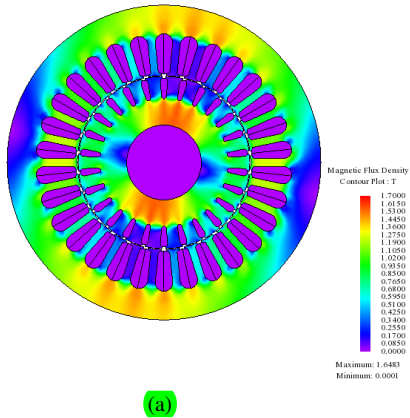
Table 1 Results of the linear simulation

$ I_D - I_A $ (A)	Radial Displacement (mm)
-0.366937291	-0.2
-0.177825511	-0.1
-3.96665e-5	0
0.177742551	0.1
0.366860792	0.2

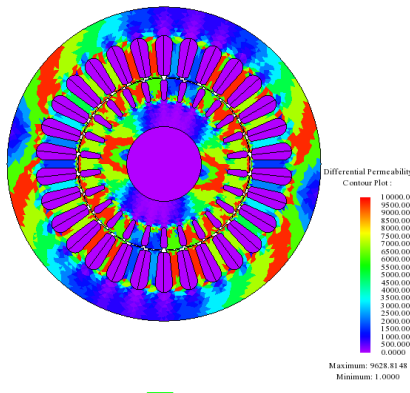
Case 1: Linear condition. In the linear simulations, the eddy current solver is selected, and the solver frequency is set at 200Hz. 0- voltage is injected in the motor, and the MF distribution is like Fig.1. The simulations are carried out under five conditions, where the rotor radial displacements are -0.2mm, -0.1mm, 0mm, 0.1mm, 0.2mm. The amplitudes of the phase currents are used to carry out the proposed method. The simulation results of the linear simulation are plotted in Tab.1.)

Case 2: Saturated condition. In the saturated simulations, the frozen permeability method is used. Firstly, the FEM model is simulated with static magnetic solver, and rated currents are applied. The direction of the magnetic field aligns with Phase A and Phase D. The differential permeability of the static simulation is frozen and imported to the eddy current simulations. The MF distribution and frozen permeability are presented in Fig.7. With the differential permeability in Fig.7, the same processes as the linear simulations are carried out, and the results are presented in Tab.2.)

From the comparison of Tab.1 and Tab.2, it can be found that the proposed method has almost the same performance under linear



(a)



(b)

Fig. 7: Saturation conditions. (a) MF distribution of the static simulation. (b) Distribution of the frozen differential permeability.

Table 2 Results of the saturated simulation

$ I_D - I_A $ (A)	Radial Displacement (mm)
-0.364441487	-0.2
-0.176608281	-0.1
-0.00017422	0
0.176474293	0.1
0.364531332	0.2

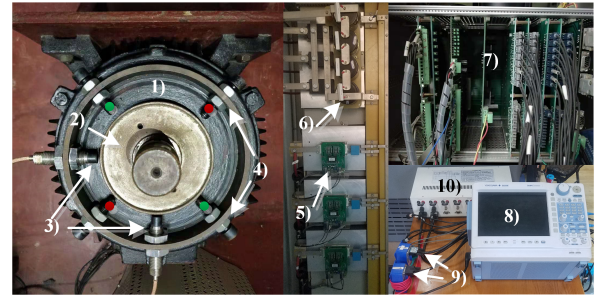
and saturated conditions, only that it is slightly more sensitive under linear condition.

4.2 Experimental Setup

To verify the proposed eccentricity detection method, a six phase bearingless induction motor is used because eccentricities can be easily created in it. The configuration of the motor is presented in Tab.3. The configurations of the experimental rig is presented in Fig.8. On the free end of the bearingless motor, a standard plate is mounted on the shaft to serve as the target for the displacement probes. It can also be seen in Fig.8(a) that four bolts are used to fix the radial displacements of the rotor for static verification. On the control board, a TMS320F28335 digital signal processor is used. The PWM carrier frequency is set at 4kHz, and the sampling rate is 8kHz. The dead time is $4\mu s$. The experiment rig has an LV25-P voltage sensor to measure the DC bus voltage, and six LAH 50-P/SP1 current sensors to measure the phase currents of the motor. For measurement instruments, an Yokogawa DL850E ScopeCorder is used. In addition, six CT200 AC/DC current probes are connected to the ScopeCorder to present the actual phase currents in rms values.

Table 3 Configuration of test motor

Rated Power	5.5kW
Pole number of the α_1 - β_1 plane	2
Core length	90mm
Outer diameter of stator	210mm
Inner diameter of stator	116mm
Air gap length	0.55mm
Clearance between shaft and touch down bearing	0.33mm



(a)

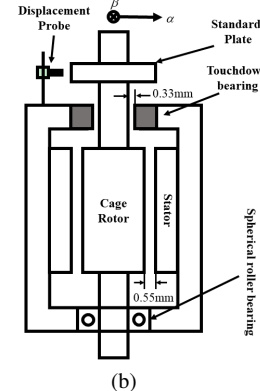


Fig. 8: (a) Experimental rig: 1)Top view of the six phase bearingless motor; 2) Standard Plate; 3) Displacement Probes; 4) Bolts for displacement fixing; 5) IGBT modules and drive circuits (six of them are used); 6) Capacitors; 7) Control board; 8) ScopeCorder; 9) CT200 Current probes (six of them are used); 10) Power supply for CT200. (b) Schematic profile of the bearingless motor.

To present the estimated displacements, an MAX5307 Digital-to-Analog converter chip is used. For radial displacement verifications, two ECDPs are mounted on the motor in the α and β directions, and their outputs are directly connected to the ScopeCorder. The waveforms of the experiment results are replotted with MATLAB.

4.3 Static Verification

In the static test, the followings can be verified: the relation between the actual and estimated displacements of the proposed method has excellent linearity; the estimations on orthogonal directions are decoupled. In the static test, the rotor is fixed with the four bolts as shown in Fig.8(a). The rotor displacements are tuned by adjusting the bolts. The four bolts can be divided into two pairs as shown in Fig.8(a). The red pair determines the common mode of d_α and d_β , the green pair determines the differential mode of d_α and d_β . According to Tab.3, the maximum radial displacement is 0.33mm. Hence, thirteen points as listed below are chosen for the static verifications.

In the experiments, the amplitude of the injected signals (V_c) is set at 20V, and the frequency of the injected signals (ω_c) is 200Hz. The rms values are measured with the CT200 current probes. The estimated radial displacements are calculated in the TMS320F28335

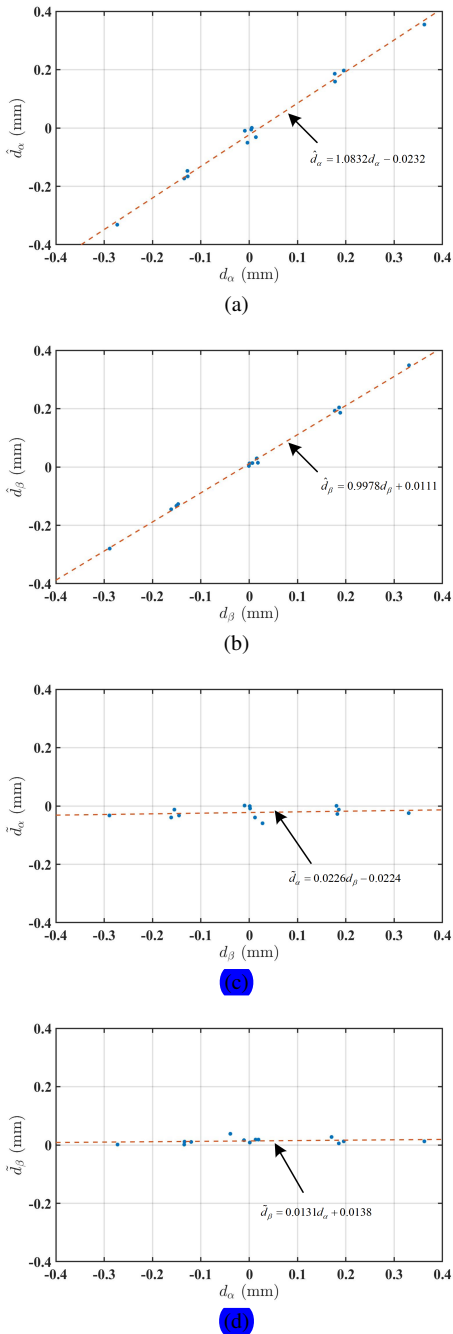


Fig. 9: Relations between estimated and measured displacements (blue dots represent the experiment results, red dashed lines are the fitting curves of the results). (a) Relation between \hat{d}_α and d_α . (b) Relation between \hat{d}_β and d_β . (c) Relation between \hat{d}_α and d_β . (d) Relation between \hat{d}_β and d_α .

with the LAH 50-P/SP1 measured currents and output with the DAC chip.

- $d_\alpha = 0mm, d_\beta = 0mm$
- $d_\alpha = 0mm, d_\beta = 0.33mm$
- $d_\alpha = 0mm, d_\beta = -0.33mm$
- $d_\alpha = 0mm, d_\beta = 0.165mm$
- $d_\alpha = 0mm, d_\beta = -0.165mm$
- $d_\alpha = 0.33mm, d_\beta = 0mm$
- $d_\alpha = -0.33mm, d_\beta = 0mm$
- $d_\alpha = 0.165mm, d_\beta = 0mm$
- $d_\alpha = -0.165mm, d_\beta = 0mm$

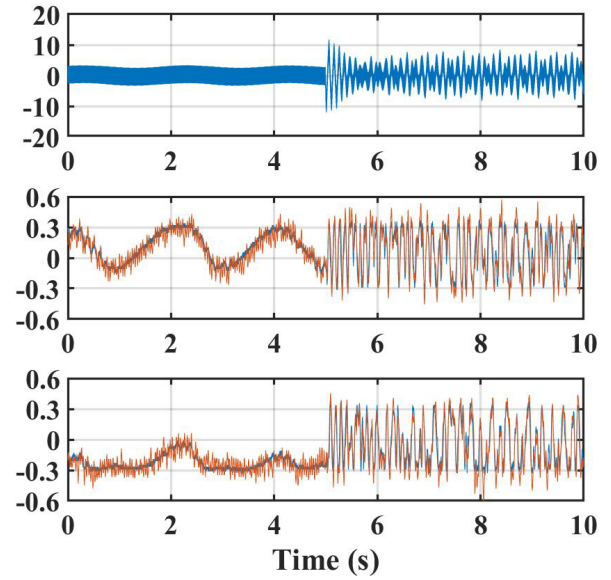


Fig. 10: Verification of the eccentricity detection under VVVF operation, waveforms from top to bottom: Phase A current (A); d_α (mm) (blue) and d_β (mm) (red); d_α (mm) (blue) and d_β (mm) (red).

- $d_\alpha = 0.165mm, d_\beta = 0.165mm$
- $d_\alpha = 0.165mm, d_\beta = -0.165mm$
- $d_\alpha = -0.165mm, d_\beta = -0.165mm$
- $d_\alpha = -0.165mm, d_\beta = 0.165mm$

The relations between the estimated displacements and the measured displacements are plotted in Fig.9 according to the test results. The fitting curve of the test points are also presented in Fig.9 with red dashed lines. It can be found from Fig.9(a) and Fig.9(b) that the relation between the estimated displacements and the measured displacements have excellent linearity with near-unity slopes and near-zero offsets. From Fig.9(c) and Fig.9(d), the slopes of the fitting curves are quite small, which means the displacement estimations are hardly affected by the actual displacements on the orthogonal directions.

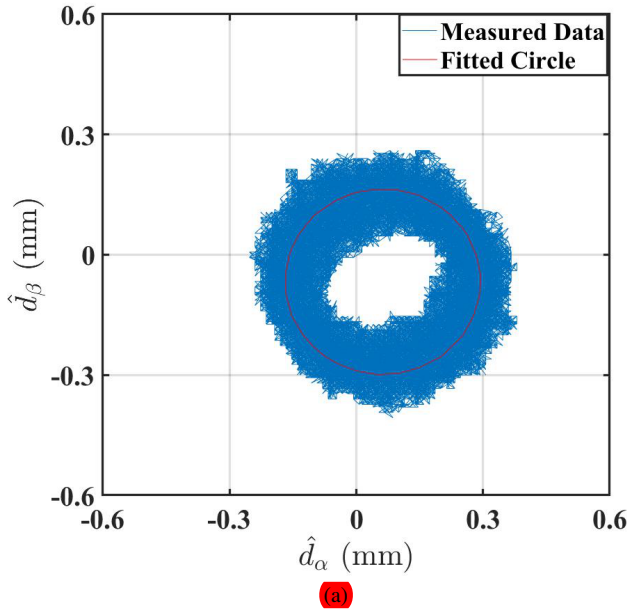
4.4 Dynamic Verification

To test the tracking bandwidth of the proposed eccentricity detection method, it is performed on the test motor under variable voltage variable frequency (VVVF) operation with the bolts all loosened. The rotor leans on the touchdown bearing and the displacements vary as alternating waves. The operation speed is switched from 150rpm to 300rpm at 3.5s. The parameters of the OGS in the demodulation strategy is $G = 0.2\pi, \omega_c = 400\pi$. The injected signals are the same as those in the static tests. It can be found from Fig.10 that the estimated displacements track the actual displacements well.

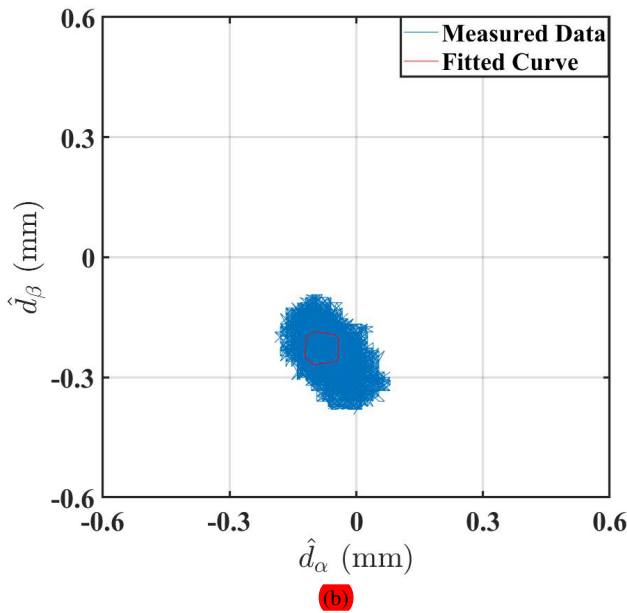
4.5 Discrimination of Eccentricity Types

The proposed method detects the radial displacements in real-time. Hence, unlike the traditional MCSA method, it is able to discriminate between different types of eccentricities. The MCSA method can only detect mixed eccentricity faults but cannot determine what percent of dynamic and static eccentricity contribute to the total eccentricity [7]. In this subsection, it will be shown with experiments that the proposed method can detect and discriminate between different eccentricities.

In order to create steady eccentric conditions, the motor is operated under VVVF control strategy of 2.5Hz and 5Hz. When no external radial forces are applied, the motor works under mixed eccentricity with dominant dynamic eccentricity. When an external



(a)



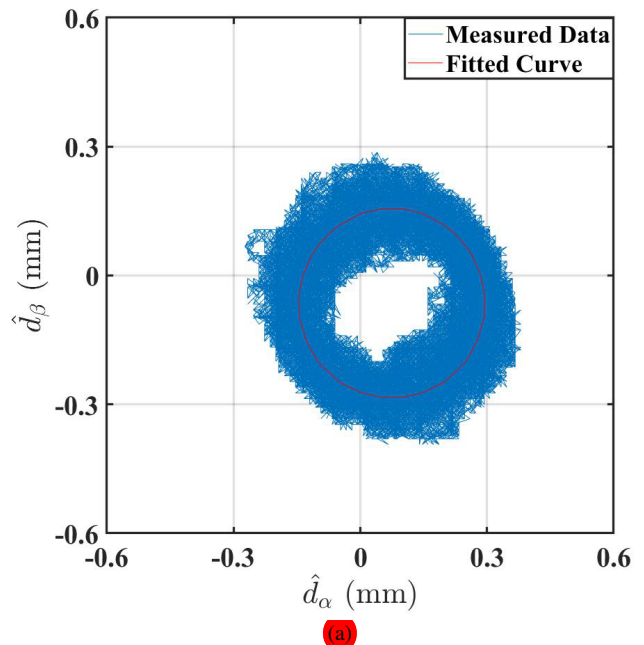
(b)

Fig. 11: $d_\alpha - d_\beta$ trajectories under 2.5Hz and their fitted curves.
 (a) No external radial force applied, center of the fitted curve: (0.0629mm, -0.0673mm), radius of the fitted curve: 0.2323mm.
 (b) External force applied, center of the fitted curve: (-0.083mm, -0.2274mm), radius of the fitted curve: 0.0509mm.

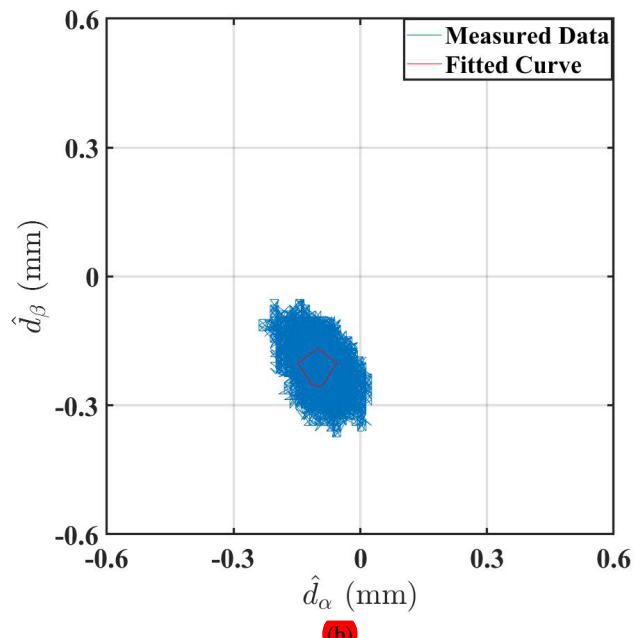
radial force is applied to the free end of the shaft, the motor works under mixed eccentricity with dominant static eccentricity.

The estimated radial displacements under 2.5Hz are plotted as $d_\alpha - d_\beta$ trajectories in Fig.11, as well as their fitted curves. In Fig.11(a), no external forces are applied on the rotor, the center of the fitted curve is (0.0629mm, -0.0673mm), and the radius of the fitted curve is 0.2323mm. Because the air-gap length is 0.33mm, the dynamic eccentricity ratio is 0.704, and the static eccentricity ratio is 0.2791. In Fig.11(b), external forces are applied on the rotor, the center of the fitted curve is (-0.083mm, -0.2274mm), and the radius of the fitted curve is 0.0509mm. Hence, the dynamic eccentricity ratio is 0.1542, and the static eccentricity ratio is 0.7336.

Similar processes are carried out under 5Hz operation, the $d_\alpha - d_\beta$ trajectories are given in Fig.12. In Fig.12(a), no external forces are applied on the rotor, the center of the fitted curve is (0.0746mm,



(a)



(b)

Fig. 12: $d_\alpha - d_\beta$ trajectories under 5Hz and their fitted curves.
 (a) No external radial force applied, center of the fitted curve: (0.0746mm, -0.0648mm), radius of the fitted curve: 0.2217mm.
 (b) External force applied, center of the fitted curve: (-0.1014mm, -0.2103mm), radius of the fitted curve: 0.0488mm.

-0.0648mm), and the radius of the fitted curve is 0.2217mm. Hence, the dynamic eccentricity ratio is 0.6717, and the static eccentricity ratio is 0.2994. In Fig.12(b), external forces are applied on the rotor, the center of the fitted curve is (-0.1014mm, -0.2103mm), and the radius of the fitted curve is 0.0488mm. Hence, the dynamic eccentricity ratio is 0.1480, and the static eccentricity ratio is 0.7076.

From the presented experimental results, it can be verified that the proposed method is capable of discriminate between different eccentricity types.

5 Conclusions

This paper proposes a novel eccentricity detection method for a six phase motor. The method exploits the 0– axis of the six phase motor for signal injections, which was seldom used in existing literatures. This injected signal is decoupled from the algorithms carried out on other planes and is capable of producing pulsating MF which excites the eccentric features of the rotor. Under HFI, the induction motor can be simplified as a model with decoupled winding pairs and the analysis of the eccentricity can be carried out on individual phases. The impedance of a single phase under HFI is derived and the proposed method is drawn accordingly. In the end, the influence of saturation on the proposed method is justified by simulations, the accuracy of the proposed method is verified with static experiments and dynamic experiments, the capability of the proposed method to discriminate between different types of eccentricities is proved. It is shown in the experiments that the proposed method has excellent linearity; the displacement estimations on orthogonal directions are decoupled from each other; the tracking bandwidth under operation is satisfactory.

6 References

- 1 T. M. Wolbank and P. E. Macheiner, "Monitoring of Static and Dynamic Air Gap Eccentricity of Inverter Fed Induction Machine Drives," *IECON 2006 - 32nd Annu. Conf. IEEE Ind. Electron.*, pp. 1504–1509, 2006. [Online]. Available: <http://ieeexplore.ieee.org/lpdocs/epic03/wrapper.htm?arnumber=4153520>
- 2 ———, "Modulation of transient reactances of induction machines caused by different types of eccentricity," *2007 IEEE Int. Symp. Diagnostics Electr. Mach. Power Electron. Drives, SDEMPED*, pp. 89–94, 2007.
- 3 B. Ebrahimi and J. Faiz, "Magnetic field and vibration monitoring in permanent magnet synchronous motors under eccentricity fault," *IET Electr. Power Appl.*, vol. 6, no. 1, p. 35, 2012. [Online]. Available: <http://digital-library.theiet.org/content/journals/10.1049/iet-epa.2010.0159>
- 4 B. M. Ebrahimi, M. J. Roshtkhari, J. Faiz, S. Member, and S. V. Khatami, "Advanced Eccentricity Fault Recognition in Permanent Magnet Synchronous Motors Using Stator Current Signature Analysis," *IEEE Trans. Ind. Electron.*, vol. 61, no. 4, pp. 2041–2052, 2014.
- 5 W. T. Thomson, S. M. Ieee, and A. Barbour, "ON-LINE CURRENT MONITORING AND APPLICATION OF A FINITE ELEMENT METHOD TO PREDICT THE LEVEL OF STATIC AIRGAP ECCENTRICITY IN THREE-PHASE INDUCTION MOTORS," *IEEE Trans. Energy Convers.*, vol. 13, no. 4, pp. 347–357, 1998.
- 6 S. Nandi and H. A. Toliat, "Detection of rotor slot and other eccentricity related harmonics in a three phase induction motor with different rotor cages," *IEEE Trans. Energy Convers.*, vol. 16, no. 3, pp. 253–260, 2001.
- 7 H. A. Toliat, S. Nandi, S. Choi, and H. Meshgin-Kelk, *Electric machines: modeling, condition monitoring, and fault diagnosis*. CRC press, 2012.
- 8 B. Ebrahimi and J. Faiz, "Diagnosis and performance analysis of three-phase permanent magnet synchronous motors with static, dynamic and mixed eccentricity," *IET Electr. Power Appl.*, vol. 4, no. 1, p. 53, 2010. [Online]. Available: <http://digital-library.theiet.org/content/journals/10.1049/iet-epa.2008.0308>
- 9 B. Ebrahimi, J. Faiz, and B. Araabi, "Pattern identification for eccentricity fault diagnosis in permanent magnet synchronous motors using stator current monitoring," *IET Electr. Power Appl.*, vol. 4, no. 6, p. 418, 2010. [Online]. Available: <http://digital-library.theiet.org/content/journals/10.1049/iet-epa.2009.0149>
- 10 A. Chiba, T. Fukao, O. Ichikawa, M. Oshima, M. Takemoto, and D. G. Dorrell, "Magnetic Bearings and Bearingless Drives," *Newnes*, vol. 14, no. 3, pp. 158–162, 1989.
- 11 T. Kuwajima, T. Nobe, K. Ebara, A. Chiba, and T. Fukao, "An estimation of the rotor displacements of bearingless motors based on a high frequency equivalent circuits," *4th IEEE Int. Conf. Power Electron. Drive Syst. IEEE PEDS 2001 - Indonesia. Proc. (Cat. No.01TH8594)*, vol. 2, pp. 725–731, 2001. [Online]. Available: <http://ieeexplore.ieee.org/lpdocs/epic03/wrapper.htm?arnumber=975408>
- 12 T. Tera, Y. Yamauchi, A. Chiba, T. Fukao, and M. A. Rahman, "Performances of bearingless and sensorless induction motor drive based on mutual inductances and rotor displacements estimation," *IEEE Trans. Ind. Electron.*, vol. 53, no. 1, pp. 187–194, 2006.
- 13 N. Tsukada, T. Onaka, J. Asama, A. Chiba, and T. Fukao, "Novel coil arrangement of an integrated displacement sensor with reduced influence of suspension fluxes for a wide gap bearingless motor," *IEEE Trans. Ind. Appl.*, vol. 46, no. 6, pp. 2304–2310, 2010.
- 14 A. Chiba and J. A. Santisteban, "A PWM harmonics elimination method in simultaneous estimation of magnetic field and displacements in bearingless induction motors," *IEEE Trans. Ind. Appl.*, vol. 48, no. 1, pp. 124–131, 2012.
- 15 E. Levi and R. Bojoi, "Multiphase induction motor drives – a technology status review," *IET Electr. Power Appl.*, vol. 1, no. 5, pp. 643–656, 2007.
- 16 E. Levi, F. Barrero, and M. Duran, "Multiphase Machines and Drives - Revisited," *IEEE Trans. Ind. Electron.*, vol. 63, no. 1, pp. 429–432, 2016. [Online]. Available: <http://ieeexplore.ieee.org/lpdocs/epic03/wrapper.htm?arnumber=7303950>
- 17 W. Kong, M. Kang, D. Li, R. Qu, D. Jiang, and C. Gan, "Investigation of Spatial Harmonic Magnetic Field Coupling Effect on Torque Ripple for Multiphase Induction Motor under Open Fault Condition," *IEEE Trans. Power Electron.*, vol. 33, no. 7, pp. 6060–6071, 2018.
- 18 C. C. Scharlau, L. F. A. Pereira, L. A. Pereira, and S. Haffner, "Performance of a five-phase induction machine with optimized air gap field under open loop V/f control," *IEEE Trans. Energy Convers.*, vol. 23, no. 4, pp. 1046–1056, 2008.
- 19 W. Kong, J. Huang, R. Qu, M. Kang, and J. Yang, "Nonsinusoidal power supply analysis for concentrated-full-pitch-winding multiphase induction motor," *IEEE Trans. Ind. Electron.*, vol. 63, no. 1, pp. 574–582, 2016.
- 20 W. Kong, R. Qu, M. Kang, J. Huang, and L. Jing, "Air-Gap and Yoke Flux Density Optimization for Multiphase Induction Motor Based on Novel Harmonic Current Injection Method," *IEEE Trans. Ind. Appl.*, vol. 53, no. 3, pp. 2140–2148, 2017.
- 21 W. Kong, J. Huang, M. Kang, and B. Li, "Research of sensorless control for multiphase induction motor based on high frequency injection signal technique," *2011 Int. Conf. Electr. Mach. Syst. ICEMS 2011*, 2011.
- 22 M. K. M. Kang, J. H. J. Huang, J.-q. Y. J.-q. Yang, and H.-b. J. H.-b. Jiang, "Analysis and experiment of a 6-phase bearingless induction motor," *2008 Int. Conf. Electr. Mach. Syst.*, no. 3, 2008.
- 23 B. Li, J. Huang, H. Liu, and Z. Hou, "Analysis and control of multiphase permanent-magnet bearingless motor with single set of half-coiled winding," *IEEE Trans. Ind. Electron.*, vol. 61, no. 7, pp. 2080–2086, 2014.
- 24 P. L. Jansen and R. D. Lorenz, "Transducerless position and velocity estimation in induction and salient AC machines," *IEEE Trans. Ind. Appl.*, vol. 31, no. 2, pp. 240–247, 1995. [Online]. Available: <http://ieeexplore.ieee.org/lpdocs/epic03/wrapper.htm?arnumber=370269>
- 25 ———, "Transducerless field orientation concepts employing saturation-induced saliences in induction machines," *IEEE Trans. Ind. Appl.*, vol. 32, no. 6, pp. 1380–1393, 1996.
- 26 D. Vryoubal, "Target Temperature Effect on Eddy-Current Displacement Sensing," pp. 6–10, 2015.
- 27 ———, "Impedance of the Eddy-Current Displacement Probe: The Transformer Model," *IEEE Trans. Instrum. Meas.*, vol. 53, no. 2, pp. 384–391, 2004.
- 28 H. A. Haus and J. R. Melcher, *Electromagnetic Fields and Energy*. Prentice Hall, 1989.
- 29 J. Huang, "Transformation Theory for ρ -pair Pole η -phase Symmetric System," *Trans. China Electrotech. Soc.*, 1995.
- 30 X. Luo, Y. Liao, H. A. Toliat, A. El-Antably, and T. A. Lipo, "Multiple Coupled Circuit Modelling Of Induction Machines," *Ind. Appl. IEEE Trans.*, vol. 31, no. 2, pp. 311–318, 1995. [Online]. Available: <http://lipo.ece.wisc.edu/1993pubs/93-59T.pdf>
- 31 J. Faiz and I. Tabatabaei, "Extension of winding function theory for nonuniform air gap in electric machinery," *IEEE Trans. Magn.*, vol. 38, no. 6, pp. 3654–3657, 2002.
- 32 T. Wang and J. Huang, "Radial position detection of five-phase bearingless PM motor," *Proc. - 2016 22nd Int. Conf. Electr. Mach. ICEM 2016*, pp. 2602–2608, 2016.
- 33 M. Ciobotaru, R. Teodorescu, and F. Blaabjerg, "A New Single-Phase PLL Structure Based on Second Order Generalized Integrator," no. June, pp. 18–22, 2006.